

Mechanical Abuse Simulation and Effect of Graphene Oxides on Thermal Runaway of Lithium ion Batteries

Cuiying Dai¹, Xiaoxue Zhu¹, Junan Pan¹, Xiangbiao Liao², Yong Pan^{1,*}

¹ School of Materials Science and Engineering, Xiangtan University, Hunan 411105, China

² Department of Earth and Environmental Engineering, Columbia University, New York 10027, USA

*E-mail: ypan@xtu.edu.cn

Received: 9 March 2018 / Accepted: 12 January 2019 / Published: 10 March 2019

The challenge of suppressing thermal runaway in lithium ion batteries (LIBs) under thermal and mechanical abuses is critical in practice applications. The graphene oxides (GOs) modified $\text{LiNi}_{0.5}\text{Mn}_{0.3}\text{Co}_{0.2}\text{O}_2$ (NMC532) active materials were prepared on aluminum foil by the coating method. Effect of different ratios of the GOs on the electrochemical cycling performance of the coin-cells was discussed. GOs affect the specific capacity of the half-cells, but they are helpful for improving the cycle stabilities of the cells. The contributions of GOs modified NMC532 cathodes on suppressing thermal runaway of LIBs were studied by nail penetration tests, impact tests and scratch tests, respectively. The temperature distribution on the coin-cell surface was in-situ monitored by FLIR infrared camera technique during nail penetration tests. The residual surface morphology of the cathodes were observed by scanning electron microscopy after impact and scratch tests. All results indicate that GOs play an important role in inducing cracking nucleation, raising internal impedance and restraining heat generation when the internal shorting occurs in LIBs.

Keywords: Graphene oxides, impact test, nail penetration test, scratch test, thermal runaway

1. INTRODUCTION

Lithium ion batteries (LIBs) have wide applications including grid energy storage, electric vehicles and electronics owing to high energy density, long cycle life and superior cost-performances [1-6]. Extensive efforts have been devoted recently to improving the specific energy and cycle life by developing new battery components [7,8]. However, the safety of LIBs remains a significant challenge [9-12]. Particularly, thermal runaway limits the applications of high energy density LIBs when they are subjected to abuse conditions [13].

The heat generation of a lithium ion battery is usually mild during normal operations, and it can be well handled by the battery thermal management systems [14,15]. However, if the circuit shorting

phenomenon caused by mechanically or thermally abuse conditions occurs, the exothermic reactions can be triggered and further induce the rapidly increasing of temperature and pressure, finally resulting in fire and explosion. Although the external components were equipped in commercial LIBs, the speed of temperature change is much higher than that detected by these devices. Therefore, some internal strategies are more effective to prevent the combustion and explosion of LIBs. There are significant efforts on designing internal components of LIBs to mitigate thermal runaway, including positive temperature coefficient materials [16,17], functional separators [18-20] and modified electrolytes [21]. These traditional internal-short mitigation strategies were designed to be effective when temperature exceeds a high value ($\sim 120\text{ }^{\circ}\text{C}$). However, it is hard for LIBs to reach such a high temperature in an instant when facing mechanical abuses in practice applications.

The triggered thermal runaway mitigation mechanisms of LIBs have attracted extensive research attentions to prevent thermal runaway when LIBs are subjected to mechanical impacts [15,22,23]. The related works were studied by introducing damage homogenizers (DH) with carbon black or carbon nanotubes along the electrode thickness [24]. As LIBs deform due to the external mechanical loading, the DH particles can trigger the widespread fractures of electrodes and then improve the internal impedance rapidly before the heat generation starts to rise. It can minimize the heat generation rate [22]. However, the mechanisms of bridging interfacial cracks and reduced heat generation remains unclear.

In this work, graphene oxides (GOs) with good hydrophilicity and dispersibility were added into the $\text{LiNi}_{0.5}\text{Mn}_{0.3}\text{Co}_{0.2}\text{O}_2$ electrode slurry as the homogenizer of electrode failure, as depicted in Fig. 1. The GOs serve as crack initiators when LIBs are subjected to mechanical abuses. The modified electrode still shows good performance on the energy density and cycle life due to the good conductivity and low density of GOs. Under mechanical abuse conditions, both impact and scratch testes show that GOs preferably debond from electrode particles and widespread cracks formed in the active material layers. The internal impedance of electrode was verified to increase with the existing of cracks. Furthermore, nail penetration, impact and scratch tests indicate the modified electrode with GOs can reduce heat generation and improving the safety of LIBs.

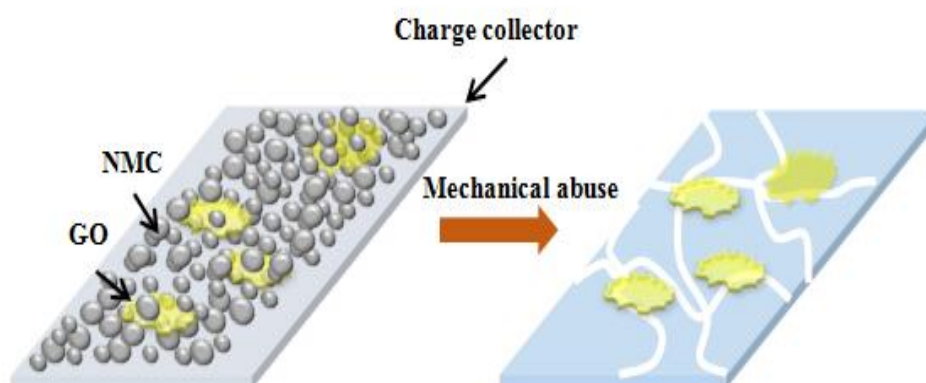


Figure 1. Schematic of GOs-modified cathodes under mechanical abuses, resulting in crack network

2. EXPERIMENTAL

2.1 Electrodes preparation

The reference positive electrode contains 93.0 wt. % $\text{LiNi}_{0.5}\text{Mn}_{0.3}\text{Co}_{0.2}\text{O}_2$ (NMC532 from KEJING, China), 4.0 wt. % polyvinylidene fluoride (PVDF, purchased from KEJING, China) and 3.0 wt. % carbon black (CB, purchased from KEJING, China) dissolved in N-methyl-2-pyrrolidone (NMP). The weight ratio of solid components is active materials (AM): PVDF: CB = 93:4:3. For anodes, the active materials are artificial graphite powders (from KEJING, China), and the weight ratio of solid components is AM: PVDF: CB = 93:6:1. The GOs (purchased from Suzhou Carbon Peak Technology Co., Ltd.) modified cathodes were prepared by adding 1.0 wt. %, 3.0 wt. %, 5.0 wt. % GOs into the same aforementioned slurry, respectively. The slurry was agitated with a magnetic stirrer until it was uniformly mixed. The mixed slurry was coated on an aluminum foil via a doctor blade method and dried in a dry box at 80 °C for 4 hours, and then dried in a vacuum oven at 80 °C for 8 hours. The thickness of electrodes was controlled about 100 μm for electrochemical tests and 200 μm for nail penetration, impact and scratch tests. The electrodes were cut into many discs with the diameter of 10 mm. The mass of NMC532 in a reference electrode film was 11.4 – 12.9 mg, while the mass of NMC532 in a modified electrode film was lower than that in the reference film, around 6.0 – 11.0 mg. The structure of the AM/GO mixed electrode was characterized by field emission scanning electron microscope (FESEM) and transmission electron micromorphology (TEM, No. JEM-2100).

2.2 Electrochemical tests

Half-cells were assembled in an argon-filled glove box with both H_2O and O_2 levels less than 0.1 ppm by sandwiching a working electrode, a porous PP/PE/PP tri-layer separator with the thickness of 25.0 μm and a lithium disc into a CR2016 coin cell. The electrolytes were 1.0 mol L^{-1} LiPF_6 in ethylene carbonate/diethyl methyl carbonate/ethyl methyl carbonate (the mass ratio is 1:1:1). Electrochemical impedance spectroscopy (EIS) measurements were performed in the frequency range from 100 kHz to 0.01 Hz on a CHI660D electrochemical station. The galvanostatic charge/discharge cycling was performed in the potential range of 3.0 – 4.5 V at 0.5 C on a CT-3008W-5V20Ma-S4 Analyzer at room temperature.

2.3 Impact test of electrodes

The impact test on electrodes was performed using Tubular Impact Tester (BGD 306), as displayed in Fig. 2(a). It includes a chief drop hammer whose weight is 1000 g, a guide with an adjustable height stop, the drop holder with the diameter of 20.0 mm and a solid stainless steel base. The force applied on the samples was determined by the drop weight and the given drop height of 8.0 mm.

2.3.2 Scratch test

A scratch test on electrodes was performed by using automatic scratch tester (BGD 520/2), as shown in Fig. 2(b). The machine consists of a diamond-made scratch nail with a diameter of 0.06 mm, three variable counterweights, two constant counterweights, balance trestle, work platform and tester base. The sample fixed on the work platform was driven with a speed of 10.0 mm/s, and then scored by the scratch nail. The force applied on the samples was evaluated by the counterweight.

2.3.3 Nail penetration test

Nail penetration tests were carried out on fully charged cells on a solid polyurethane platform, as shown Fig. 2(c). The cells are firmly attached on the platform and penetrated by a stainless nail with the diameter of 1.2 mm.

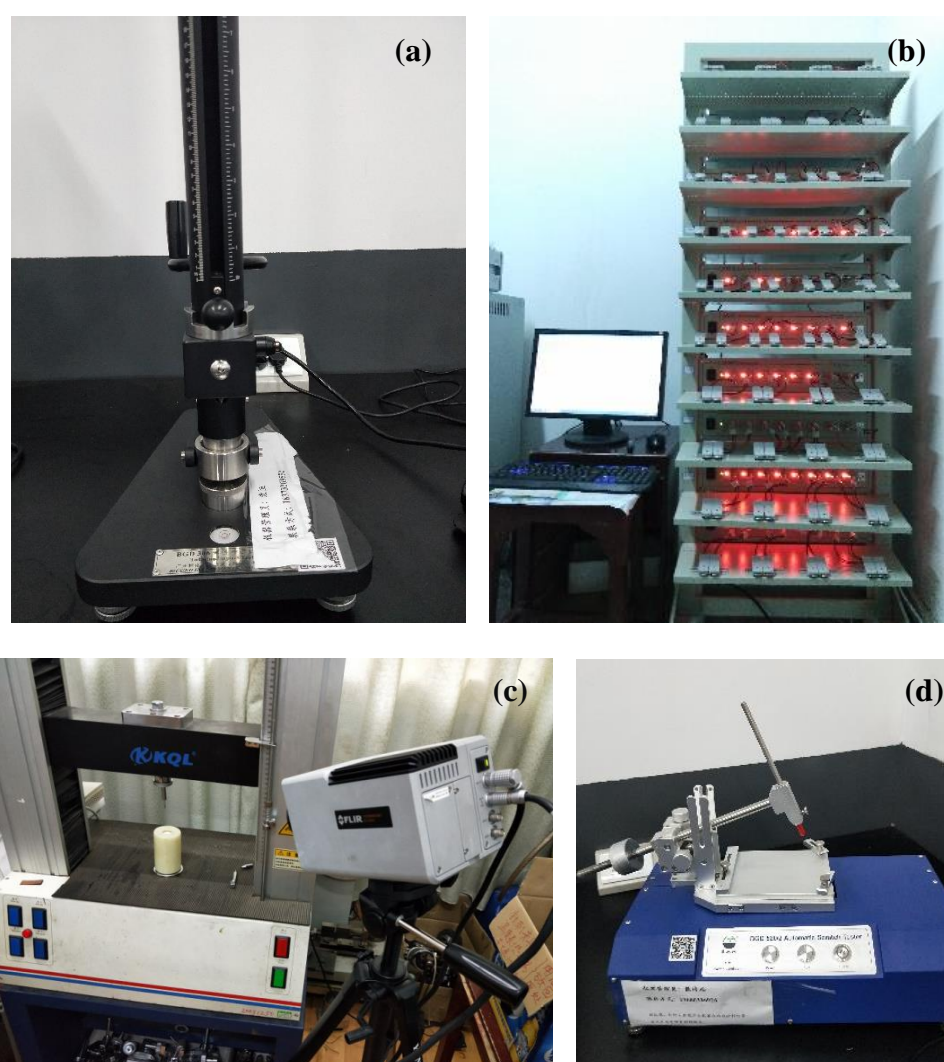


Figure 2. Optical images of experimental apparatus, (a) impact test, (b) electrochemical test, (c) nail penetration test, (d) scratch test.

The nail is attached to the jig of microcomputer controlling electronic universal tensile testing machine (No. WDT11-5) and driven at the speed of 50.0 mm/min. A FLIR infrared camera was used to in situ monitor the temperature evolution of the cell surface during the tests. The distance from the camera lens to the cell surface is about 8.5 cm (see Fig. 2(d)). The sampling frequency of the infrared system is set as 0.2 s for each image.

3. RESULTS AND DISCUSSION

Fig. 3(a) shows the FESEM observation of the structure morphology of the GOs modified electrode. It can be seen that the active material particles are closely packed, which are conformably coated by GOs. It is also found the wrinkling behavior of graphene due to the ultrathin nature. The GOs change the morphology and size of metal oxides, similar to the previous data [25-27]. The HRTEM image of the GOs modified electrode in Fig. 3(b) further confirms that the excellent graphene coating and graphene oxides nanosheets with a lattice spacing of about 0.417 nm is mixed successfully. The total layer number of GOs is evaluated as 10. So the total thickness of GOs is about 4.0 nm. The dense GOs additives can provide not only good electrochemical stability but also crack initiators, which is useful for increasing the shorting resistance of LIBs.

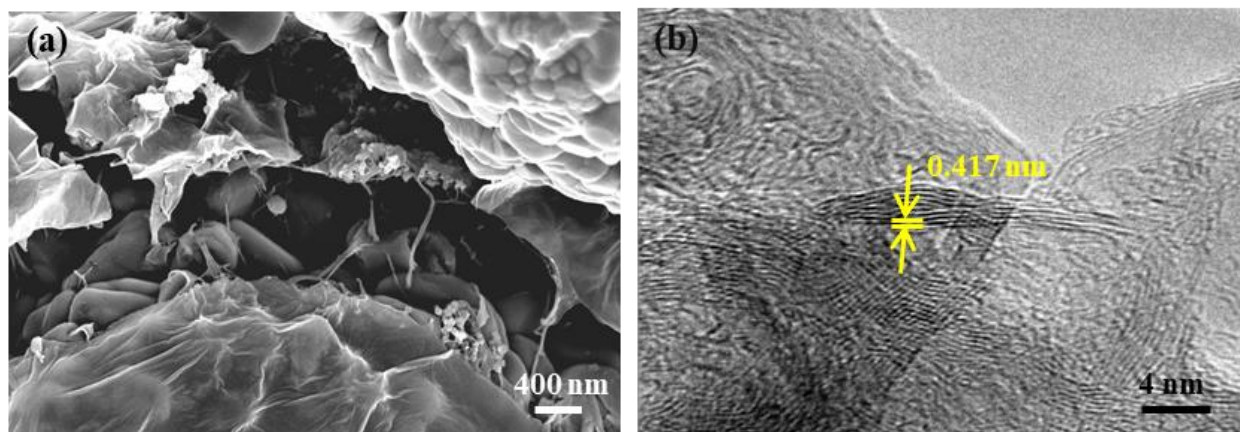


Figure 3. Micro-structure analysis of GOs-modified cathodes. (a) FESEM image of cathodes particles. (b) HRTEM image of the conformal graphene oxide film on NMC532 particles.

It is seen from Fig. 4(a) that although the GOs affect the specific capacity of the half-cells, they are helpful for improving the cycle stabilities of the cells. Especially, the modified sample of GOs with 5.0 wt. % exhibits excellent cycling stability. It can be attributed to the superior flexibility of GOs, which can hinder the migration and storage of lithium ions. In addition, the specific capacity of the modified cathode with 1.0 wt. % GOs is higher than those with 3.0 wt. % and 5.0 wt. %. The main reason may be ascribed that the greater weight of the GOs component would further decrease the weight of the active materials. It results in the degradation of specific capacity of the half-cells.

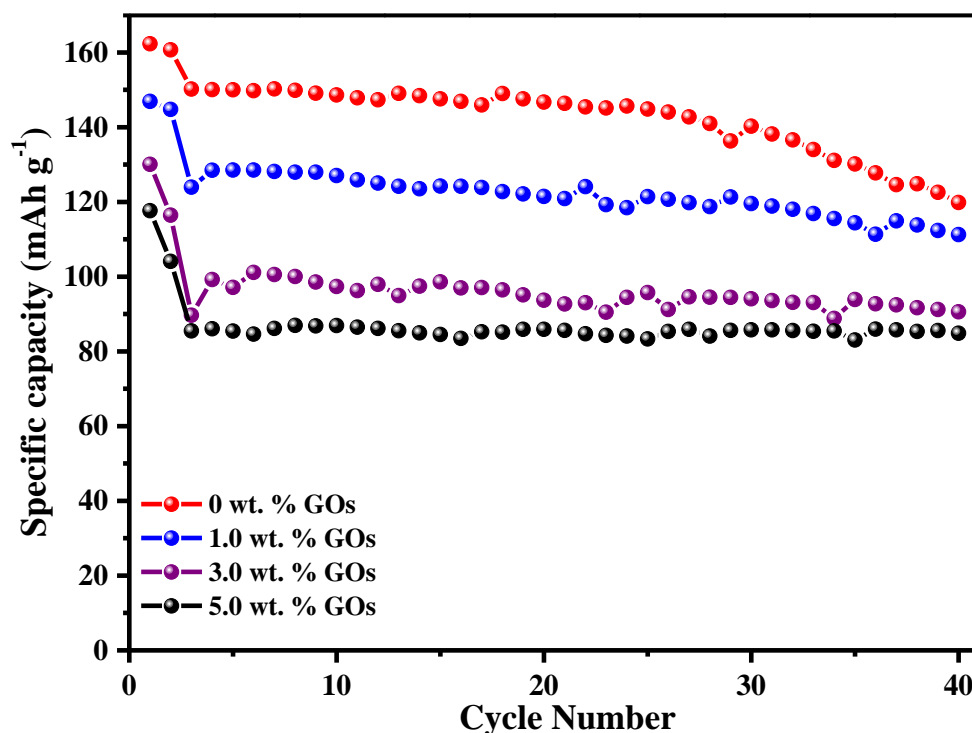


Figure 4. Cycle performances of the reference and different GOs-modified cathodes in half cells at 0.5 C.

As we know, the membrane separator in LIBs can keep the cathode and anode electrically uncontact in practical working conditions. However, for the nail penetration tests, the membrane separator is broken by the stainless nail which provides an electrically conductive shorting path between the cathode and anode. The internal shorting causes large current and further induces the rapid rate of heat generation. In the present work, the FLIR Infrared camera was used to in situ capture the details of temperature evolution corresponding to the short circuit during nail penetration tests, as shown in Fig. 5. It can be seen that a core region with high value ($> 16\text{ }^{\circ}\text{C}$) occurs and it is surrounded by low temperature region for four temperature distribution patterns. Noted that the size of the core region of the temperature field for the reference cathodes is much larger than that for the GOs modified cathodes. It indicates that the greater the size is, the more obvious the heat generation is. Here, the 5.0 wt. % GOs modified cathodes present the smallest core region. The greater GOs would be helpful for debonding occurred among the active material particles and cracking formation. Therefore, the GOs play an important role in promoting interface cracking nucleation and propagation, enhancing the internal impedance and reducing the magnitude of heat generation during the mechanical abuse analysis.

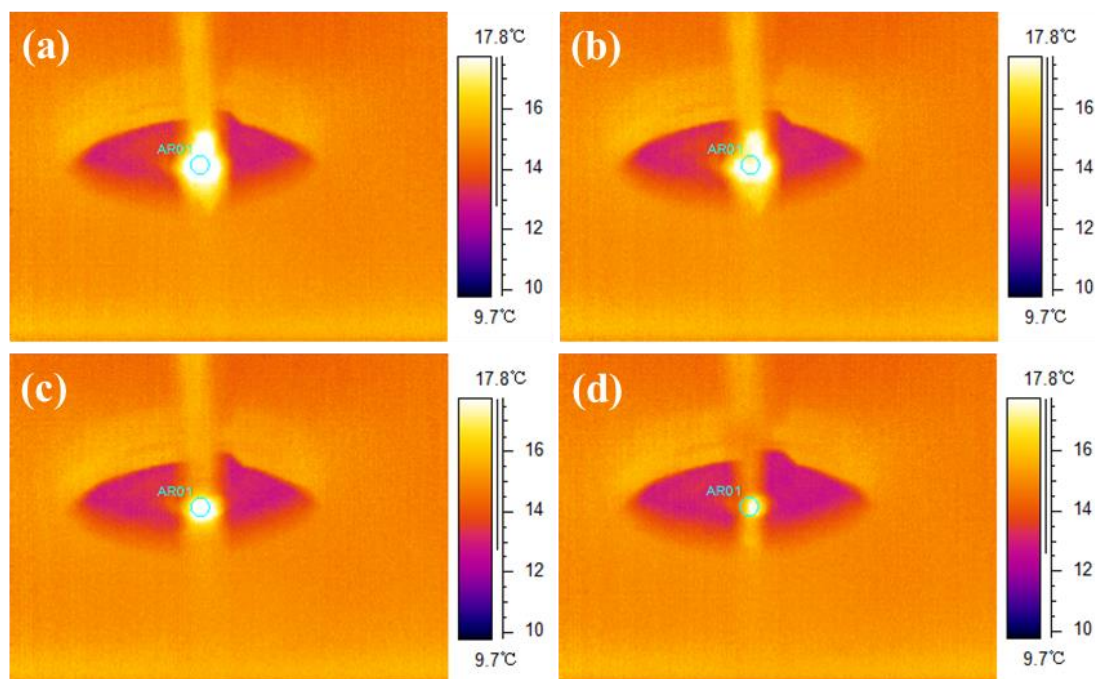


Figure 5. Images of temperature distributions on the cell surface at 2.4 s, (a) 0 wt. % GOs, (b) 1.0 wt. % GOs, (c) 3.0 wt. % GOs, (d) 5.0 wt. % GOs.

Fig. 6 shows the temperature evolutions on the cell central surface when LIBs are subjected to nail penetration loads. It can be observed that the temperature profile varies markedly. The maximum temperature increment quickly grows up to about 7.5 °C within 2.0 s for all coin cells upon short circuit, which is similar to the available data [23,24]. The maximum temperature increment is about 4.0 – 6.0 °C for the coin-cells during nail penetration tests [23,24]. The slight difference may be attributed to the different needle diameters, the penetration depths and the needle speeds and the temperature measurement tools. The heat generation declines when the increased temperature spreads to other regions. The temperature increment gradually decreases and becomes a time-dependent constant within 10 s because the stored electrical energy in LIBs is consumed. Compared with the previous results [15,23,24], the temperature drop rate during nail penetration tests is faster because no thermal insulation device is used in our experiments. The ambient temperature is low, which accelerates the loss of heat. A modified compressive and torsion experimental method was applied to analyze the internal short circuit of commercially available large-format 18 Ahr LiFePO₄ (LFP) and 25 Ahr Li(NiMnCo)_{1/3}O₂ (NMC) cells induced by mechanical abuse, respectively. The small temperature rises to 30 – 60 °C [28]. It is interesting to find from Fig. 6 that the temperature decreasing rate in the modified cell is larger than that in the reference cell. It is biggest for the 5.0 wt.% GOs-modified cathodes. It proves that the GOs act as DH role and they are useful for forming more interface cracking, which rises the internal impedance of LIBs, and restraints the shorting current and heat generation. Finally, it would improve the safety of LIBs.

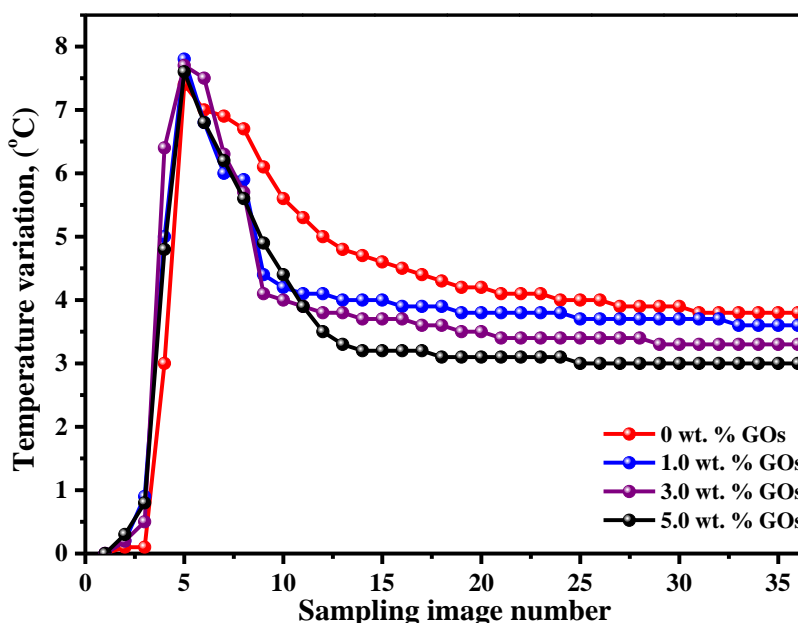


Figure 6. Measurements of temperature variation on the central region of the cell surface for the reference and different GOs-modified cathodes during nail penetration tests.

To further explore the DH effect of GOs, both impact and scratch tests were performed to simulate mechanical abuses. The surface morphologies of the modified electrodes with 0 wt. %, 1.0 wt. %, 3.0 wt. % and 5.0 wt. % GOs after impact tests are shown in Figs. 7(a)-(d), respectively. It is hardly found cracking on the reference cathode surface. But several apparent network cracks with the width range from 100 to 200 μm form on the GOs modified cathode surface. The results also agree well with the previous data [22], but the DH used in that compact test is multiwall carbon nanotube (MWCNT), the cracks in the cathode with additional MWCNT occur at the center of all electrodes [22]. In our compact tests, it is interesting to observe that the crack density on the GOs modified cathode surface after impact tests is larger than that of the reference cathode. The results indicate that the GOs additive is useful for forming interface cracking when LIBs are subjected to some mechanical abuses.

Fig. 8 shows the FESEM images of fracture morphology of different types of cathode surfaces after scratch tests. The width of the residual scratch increases with the increasing the content of GOs in cathodes under the same loads. The active materials on the both sides of the residual scratch for the reference cathode are almost intact. But for the GOs modified cathodes, more fracture phenomena of the active materials occur along the residual scratch. It also indicates that the material characterization of the active layer with different GOs additive may change from ductile to brittle features. Thus, it further verifies that GOs are good crack initiator to improve the internal impedance when LIBs undergo impact or dynamic loads.

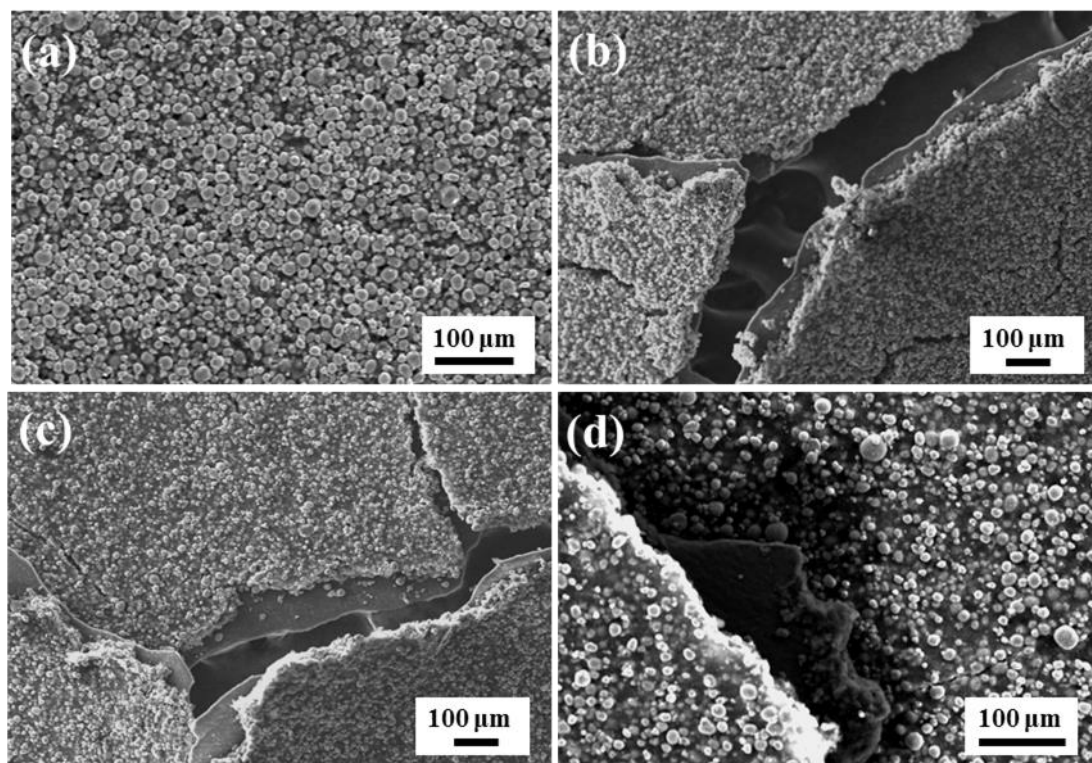


Figure 7. FESEM images of electrode films after impact tests, (a) 0 wt. % GOs, (b) 1.0 wt. % GOs, (c) 3.0 wt. % GOs, (d) 5.0 wt. % GOs.

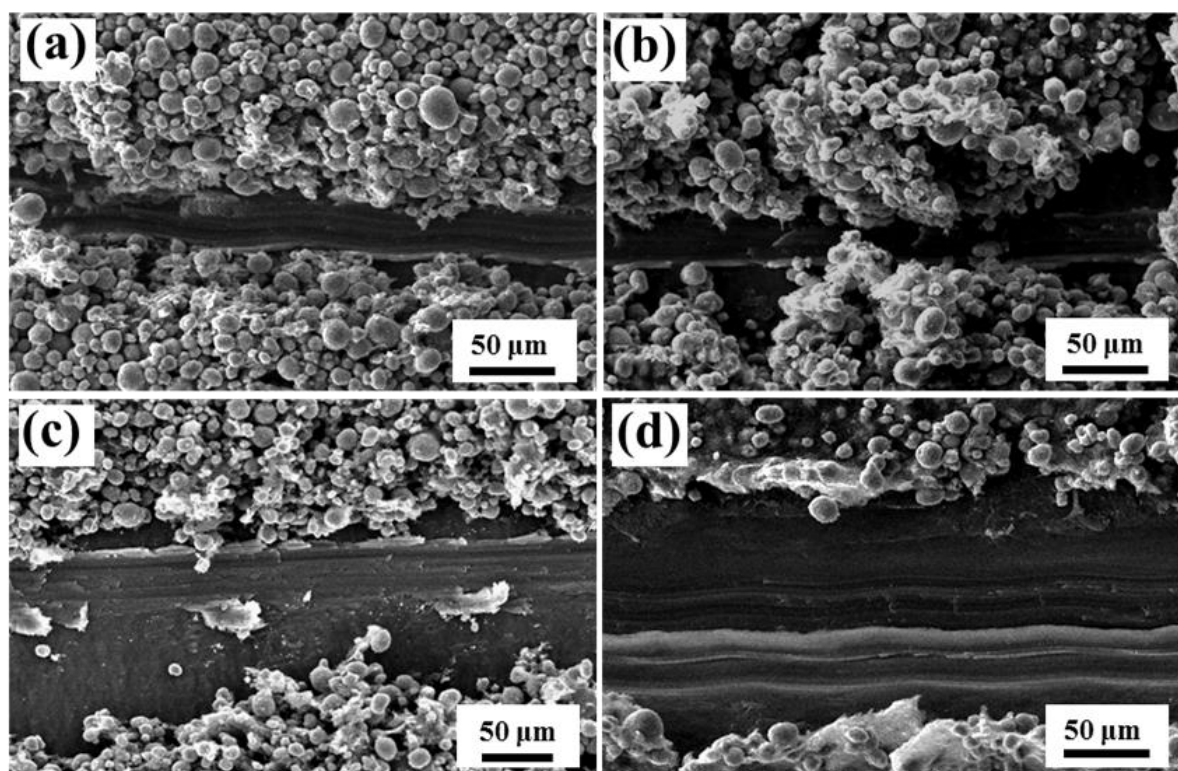


Figure 8. FESEM images of residual scratch morphology on the electrode surface after scratch tests, (a) 0 wt. % GOs, (b) 1.0 wt.% GOs, (c) 3.0 wt. % GOs, (d) 5.0 wt. % GOs.

In order to analyze the effect of the crack network formed in the aforementioned scratch tests on the internal impedance of half-cells, the home-made electrode films with crack patterns are assembled into coin cells. The crack-free cathodes and the patterned electrodes with artificial cracks are shown in Fig. 9(a). Fig. 9(b) shows the Nyquist plots of the 0 wt. % and 1.0 wt. % GOs modified cathodes with crack-free and patterned electrodes, respectively. The analysis shows that the charge transfer resistance, R_{ct} , of the reference cathode is about 60.0 Ω and it is slightly lower than $\sim 80.0 \Omega$ for 1.0 wt. % GOs-modified cathodes.

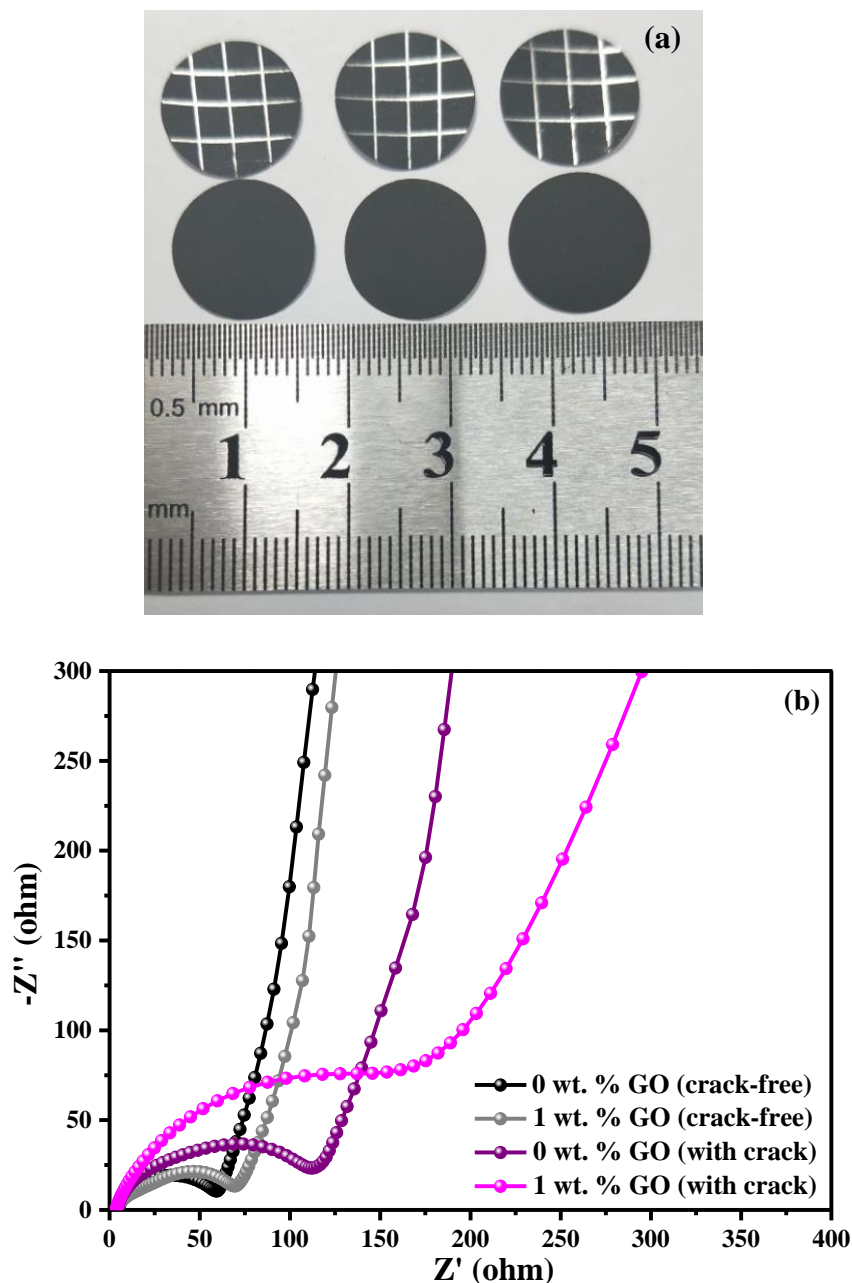


Figure 9. (a) Optical image of crack-free and patterned cathodes with artificial cracks, (b) Electrochemical impedance spectra of crack-free and patterned cathodes with 0 wt. % and 1.0 wt. % GOs, respectively.

The corresponding specific capacity of the reference cathode is better than that of 1.0 wt. % GOs-modified cathode, as shown in Fig. 4. The difference should be ascribed to the presence of GOs nanosheets, which is less conductive than CB. However, the R_{ct} value of the patterned reference cathode is about 120.0 Ω and it is much higher than that of the corresponding crack-free cathode. The R_{ct} value of the patterned 1.0 wt. % GOs-modified cathode is about 200.0 Ω . Therefore, the existed crack pattern results in the increasing of the resistance, which blocks the conducting path of electrons. It may further reduce the heat generation or the core region size of temperature field during nail penetration tests, as proved in Fig. 5. In general, GOs are excellent candidate materials as DH to suppress thermal runaway when cells are subjected to mechanical abuses.

4. CONCLUSIONS

The electrochemical performances of the reference and GOs modified NMC532 cathodes were measured. In order to explore the effect of GOs on the thermal runaway of cathodes, the coin-cells and cathodes were subjected to different type of mechanical abuses including nail penetration, impact and scratch tests in this work. The main conclusions can be summarized as follows,

1. FESEM and HETEM observations show that the active material particles are closely packed by GOs with the thickness of 4.0 nm.
2. It is found that the greater GOs affect the specific capacity of the half-cells, but they are helpful for improving the cycle stabilities of the cells.
3. The temperature distributions on the coin-cell surface were in-situ monitored by FLIR infrared camera technique during nail penetration tests. The maximum temperature increment achieves about 7.5 °C.
4. The infrared tests indicate that the greater GOs additive has more influence on the temperature variations of coin-cells during nail penetration tests. It means that GOs play an important role in restraining the heat generation when the internal shorting occurs in LIBs.
5. The results during impact tests indicate that the GOs additive is useful for forming interface cracking when the cathodes are subjected to external loads.
6. The analysis of residual scratches after scratch tests presents that GOs would change the ductile and brittle features of the NMC532 cathodes. It is a good crack initiator to improve the internal impedance when LIBs undergo scratch loads.

ACKNOWLEDGEMENTS

This work was supported by the National Natural Science Foundation of China (Grant Nos. 11372267, 11572277, 11772287, 11802260) and the Young and Middle-aged Scholar Training Program of Hunan Province Association for Science and Technology (2017TJ-Q02), the Hunan Natural Science Foundation of Hunan Province (No. 2018JJ3490).

References

1. G. Zubi, G. V. Fracastoro, J. M. Lujano-Rojas, K. El Bakari, D. Andrews. *Renew. Energy*, 132

- (2019) 1425.
2. L. X. Zhang, Z. Sun, Q. Chang, J. M. Shi, J. C. Feng. *Ceram. Int.*, 45 (2019) 1698.
 3. H. Xu, C. Wan, L. Sang, J.-P. Ao. *J. Cryst. Growth*, 505 (2019) 59.
 4. C. Xu, L. Weng, L. Ji, J. Zhou. *Eur. J. Mech. A-solid*, 73 (2019) 47.
 5. K. Wang, S. Pei, Z. He, L.-a. Huang, S. Zhu, J. Guo, H. Shao, J. Wang. *Chem. Eng. J.*, 356 (2019) 272.
 6. T. Terasako, S. Obara, S. Sakaya, M. Tanaka, R. Fukuoka, M. Yagi, J. Nomoto, T. Yamamoto. *Thin Solid Films*, 669 (2019) 141.
 7. M. Broussely, J. P. Planchat, G. Rigobert, D. Virey, G. Sarre. *J. Power Sources*, 68 (1997) 8.
 8. L. Sun, Y. Zhang, H. Si, Y. Zhang, J. Liu, J. Liu, Y. Zhang. *Electrochim. Acta*, 297 (2019) 319.
 9. J. Zhu, T. Wierzbicki, W. Li. *J. Power Sources*, 378 (2018) 153.
 10. Y. J. Nam, D. Y. Oh, S. H. Jung, Y. S. Jung. *J. Power Sources*, 375 (2018) 93.
 11. Q. Wang, L. Jiang, Y. Yu, J. Sun. *Nano Energy*, 55 (2019) 93.
 12. H. Xu, J. Shi, G. Hu, Y. He, Y. Xia, S. Yin, Z. Liu. *J. Power Sources*, 391 (2018) 113.
 13. K. Yang, X. Liu, L. Lu, S. Wang, P. Liu. *J. Power Sources*, 302 (2016) 1.
 14. S. Panchal, I. Dincer, M. Agelin-Chaab, R. Fraser, M. Fowler. *Int. J. Heat Mass Transfer*, 101 (2016) 1093.
 15. A. V. Le, M. Wang, Y. Shi, D. J. Noelle, Y. Qiao. *J. Phys. D: Appl. Phys.*, 48 (2015) 385501.
 16. H. Zhong, C. Kong, H. Zhan, C. Zhan, Y. Zhou. *J. Power Sources*, 216 (2012) 273.
 17. X. M. Feng, X. P. Ai, H. X. Yang. *Electrochem. Commun.*, 6 (2004) 1021.
 18. X. Huang. *J. Solid State Electr.*, 15 (2011) 649.
 19. E. P. Roth, D. H. Doughty, D. L. Pile. *J. Power Sources*, 174 (2007) 579.
 20. S. S. Zhang. *J. Power Sources*, 164 (2007) 351.
 21. D. H. Doughty, E. P. Roth. *Electrochem. Soc. Interface*, 21 (2012) 37.
 22. A. V. Le, M. Wang, Y. Shi, D. Noelle, Y. Qiao, W. Lu. *J. Appl. Phys.*, 72 (2015) 968.
 23. M. Wang, A. V. Le, D. J. Noelle, Y. Shi, H. Yoon, M. Zhang, Y. S. Meng, Y. Qiao. *Int. J. Damage Mech.*, 27 (2018) 74.
 24. M. Wang, A. V. Le, Y. Shi, D. J. Noelle, H. Yoon, M. Zhang, Y. S. Meng, Y. Qiao. *J. Mater. Sci. Technol.*, 32 (2016) 1117.
 25. Z. Yang, Y. Huang, F. Yao, H. Luo, Y. Wan. *Ceram. Int.*, 44 (2018) 20656.
 26. J. Li, S. H. Luo, Y. Sun, J. Li, J. Zhang, T. F. Yi. *Ceram. Int.*, (2018) In Press.
 27. C. Yang, Y. Qing, K. An, Z. Zhang, L. Wang, C. Liu. *Mater. Chem. Phys.*, 195 (2017) 149.
 28. H. Wang, E. Lara-Curzio, E. T. Rule, C. S. Winchester. *J. Power Sources*, 342 (2017) 913.